FRONTIERS OF PHYSICS

RESEARCH ARTICLE
Volume 21 / Issue 6 / 065204 / 2026

High-precision passive sensing with large-scale programmable metasurface

Zhiqiao Han [1,2,*], Qian Ma [1,2,*,†], Ze Gu [1,2], Tie Jun Cui [1,2,3,‡]

1 State Key Laboratory of Millimeter Waves, Southeast University, Nanjing 210096, China
2 Institute of Electromagnetic Space, Southeast University, Nanjing 210096, China
3 Suzhou Laboratory, Suzhou 215004, China
*These authors contributed equally to this work.
Corresponding authors. E-mail: †maqian@seu.edu.cn, ‡tjcui@seu.edu.cn
Received August 25, 2025; accepted April 20, 2026

ABSTRACT

With the rapid development of sixth-generation (6G) intelligent wireless networks, environmental sensing has become a core requirement for many applications such as autonomous driving, drones, and intelligent robotics. Here, we propose a passive sensing method based on beam-focusing algorithms and a large-scale programmable metasurface composed of 64 × 96 effective elements. The coding patterns on the 1-bit programmable metasurface are dynamically switched via a field-programmable gate array (FPGA) to achieve real-time beam focusing and scanning at specific spatial locations. The reflected signal strength is then used to determine the target angle and distance. Requiring only a single RF channel and signal strength information, the system features a simple hardware architecture and low computational complexity. To verify the effectiveness and robustness of the proposed method, experiments are conducted across 74 positions within an azimuth-angle range from –70° to 70° and a distance range from 1 m to 3 m. The experimental results demonstrate that the proposed sensing method achieves high precision in both angle and distance for passive targets, with an average absolute angle error of 0.904° and an average absolute distance error of 0.101 m. The proposed system provides a promising solution for applications in the Internet of Things, directional communication, and biomedical fields.

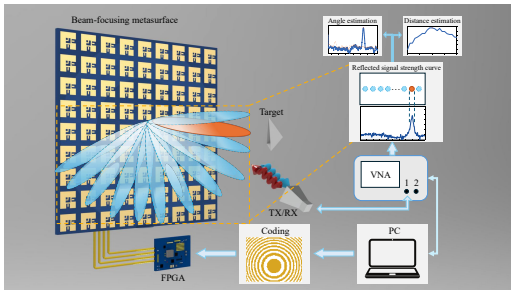

Keywords programmable metasurface, beam focusing, angle and distance estimation, passive target

1 Introduction

In recent years, electromagnetic metamaterials and their two-dimensional counterparts, metasurfaces, have attracted widespread attention due to their powerful capabilities for manipulating electromagnetic waves [1–8]. In 2014, Cui *et al.* [9] proposed the concepts of coding metamaterials and programmable metasurfaces, representing individual metasurface elements with different functionalities via digital codes. This encoding approach streamlines metasurface design and links physical implementation with information science. By incorporating active components, the metasurface can be dynamically

*Special Topic: Advances in Metamaterials: From Theory to Applications Enabled by Functional Units (Eds.: Huanyang Chen, Minghui Lu & Yangyang Fu).

Higher Education Press

https://doi.org/10.15302/frontphys.2026.065204

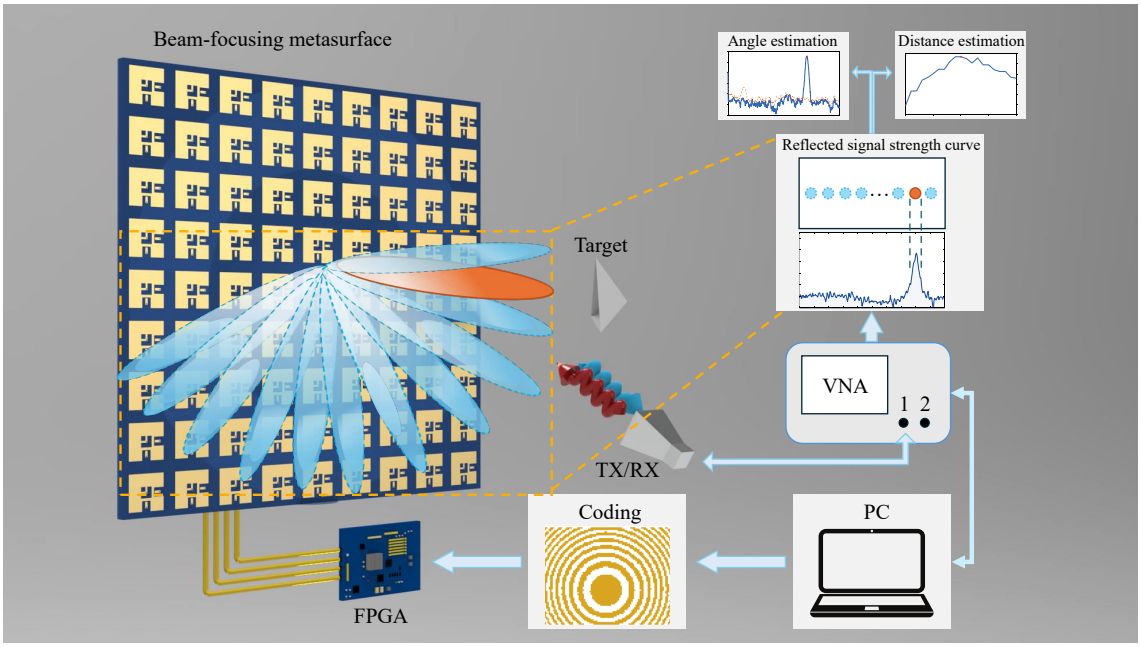

Fig. 1 Conceptual illustration of the passive target sensing method based on beam-focusing and a programmable metasurface. The FPGA dynamically reconfigures the metasurface's coding in real time to perform focused beam scanning, and the target angle and distance are inferred via peak detection of the reflected signal strength.

reconfigured via a field-programmable gate array (FPGA), enabling high flexibility and adaptability [10–14]. Consequently, numerous high-performance, low-cost, and low-profile programmable metasurface systems have been proposed for applications such as wireless communications [15–17], dynamic holography and imaging [18, 19], information processing [20, 21], and computing [22–25].

On the other hand, environmental sensing is a crucial technology in intelligent wireless systems. Accurate target detection and localization, particularly the direction-of-arrival (DOA) estimation, constitute key components of environmental sensing. However, conventional sensor-array-based signal processing methods, such as beamforming algorithms [26], Multiple Signal Classification (MUSIC) [27], and Estimating Signal Parameters via Rotational Invariance Techniques (ESPRIT) [28], often entail high hardware complexity and elevated cost, thereby constraining their applications in the next-generation intelligent wireless systems. Recently, research on DOA estimation based on programmable metasurfaces has attracted widespread attention [29–35]. Compared with the traditional sensor-array-based sensing methods, metasurfaces offer advantages such as simple hardware architecture, compact size, and low cost, making them particularly well suited to the requirements of modern intelligent systems and providing a novel solution to achieve high-precision environmental sensing.

Currently, the research on DOA estimation based on metasurfaces is mainly focused on sensing active targets, but in many critical applications such as autonomous driving, environmental monitoring, and military reconnaissance, the targets are often passive. In this paper, we present a passive target sensing method that combines the beam-focusing algorithm with a programmable metasurface, enabling not only azimuth estimation but also distance perception within a unified framework. An FPGA is used to reconfigure the metasurface's coding pattern in real time, enabling spatially focused beam scanning. The strength of the reflected signal is obtained using a transmit-receive integrated antenna, and the target azimuth angle and distance are perceived through peak detection. To validate the method, experiments are conducted at 74 test positions covering azimuths from –70° to 70° and distances from 1 m to 3 m. The results show an average absolute angle estimation error of 0.904° and an average absolute distance estimation error of 0.101 m. We envision that this work may introduce a simple architecture for target sensing leveraging the programmable metasurfaces, offering broad prospects for future development.

2 Principle and method

We propose a passive target sensing method based on beam focusing and a programmable reflective metasurface, as schematically shown in Fig. 1. The metasurface is composed of 1-bit coding elements whose reflection phase takes values of 0 or π in the "0" and "1" states, respectively. During operation, the transmit-receive antenna illuminates the metasurface, which then focuses

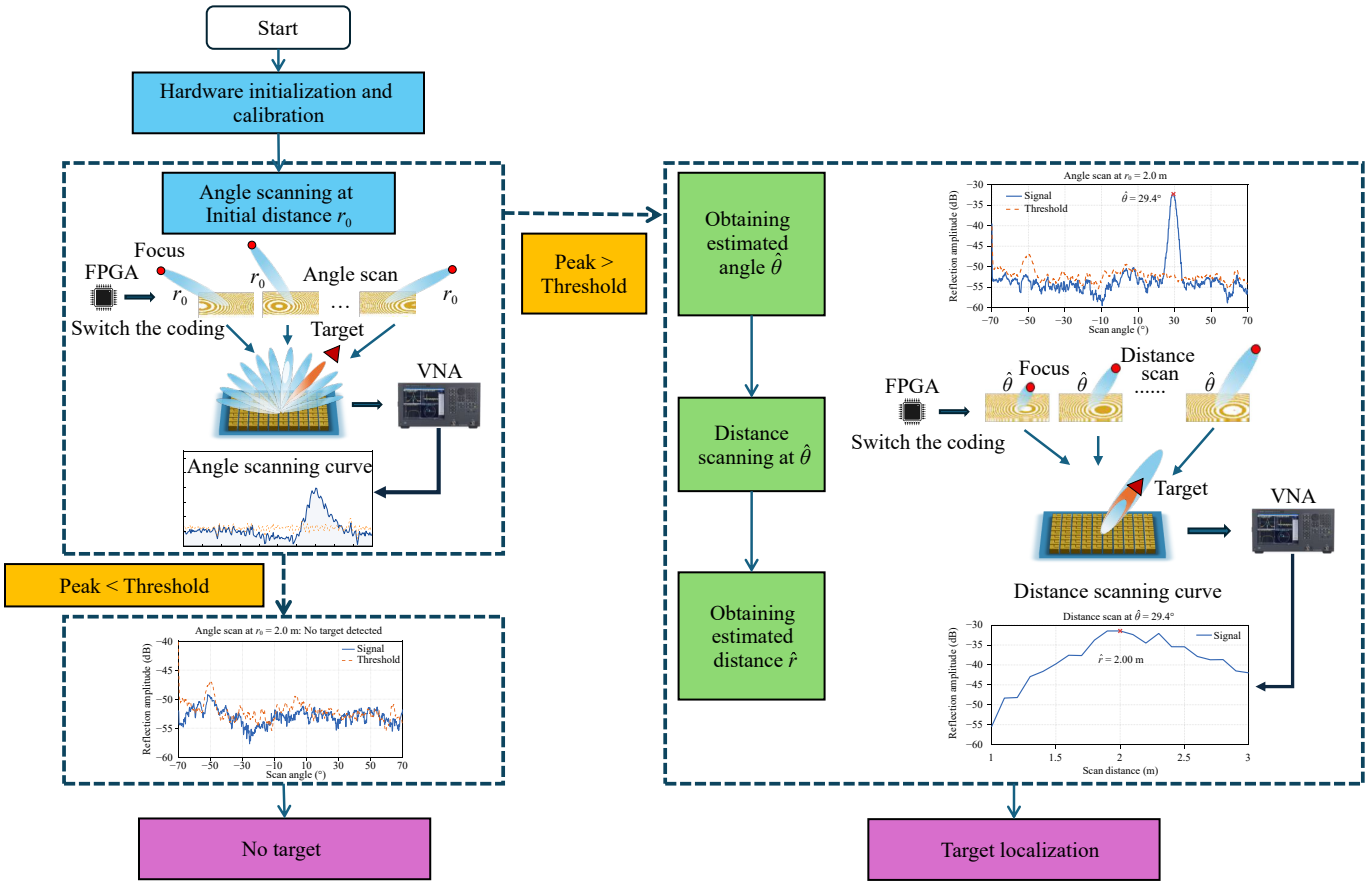

Fig. 2 Workflow diagram of the proposed method. The calibration phase comprises noise acquisition and threshold construction. First, the initial focal distance is fixed at 2 m, and an angular scan is performed. The peak of the scanning curve is compared to the corresponding noise threshold to determine whether a target is present or not. If a target is detected, the angle at which the peak occurs is taken as the estimated azimuth. The focus is then held at this angle, and a subsequent distance scan is conducted. A second peak-detection step on this distance scan then yields the estimated distance.

the wave on the preset focal point. If a target occupies the focal point, the antenna receives a strong return signal. An FPGA dynamically switches the phase state of each element, enabling the focused beam to scan across angles or distances. A personal computer (PC) acquires the reflected signal strength via the vector network analyzer and estimates the target azimuth and distance by peak-searching. The core of beam focusing lies in applying precise phase compensation to each element so that all reflected waves interfere constructively at the prescribed focal point. Let (x_i, y_i, z_i) denote the spatial position of the ith metasurface element and (x_f, y_f, z_f) the spatial position of the focal point. Then the total phase shift required for the ith unit $\phi_{total(i)}$ becomes

$$\begin{aligned}\phi_{total(i)} &= -\phi_{in(i)} + \phi_{comp(i)} \\ &= -\phi_{in(i)} + k_0\sqrt{(x_i - x_f)^2 + (y_i - y_f)^2 + (z_i - z_f)^2},\end{aligned} \tag{1}$$

where $\phi_{in(i)}$ denotes the incident wave phase at the ith element, $\phi_{comp(i)}$ is the compensation phase for focusing, and k_0 is the free-space wave number. Based on the above expressions, the total phase shift required for each metasurface element can be calculated to focus the feed-antenna's incident wave at the desired point. After 1-bit quantization, the corresponding coding patterns are obtained.

To achieve efficient passive-target sensing within the prescribed detection region, defined by azimuth angles from –70° to +70° and distances from 1 m to 3 m, this paper proposes the automated workflow shown in Fig. 2. First, the focal distance is fixed at 2 m, and the azimuth angle is swept from –70° to 70° in 0.2° increments. At each focal angle, the reflection coefficient S11 is measured at 201 frequency points within the 3.3–3.5 GHz band using a vector network analyzer. The magnitudes of the measured S-parameters are stored in a computer and averaged to yield the mean reflected strength for that angle. By employing multi-point sampling and averaging around the metasurface's center operating frequency of 3.4 GHz, the influence of measurement errors and random noise is suppressed,

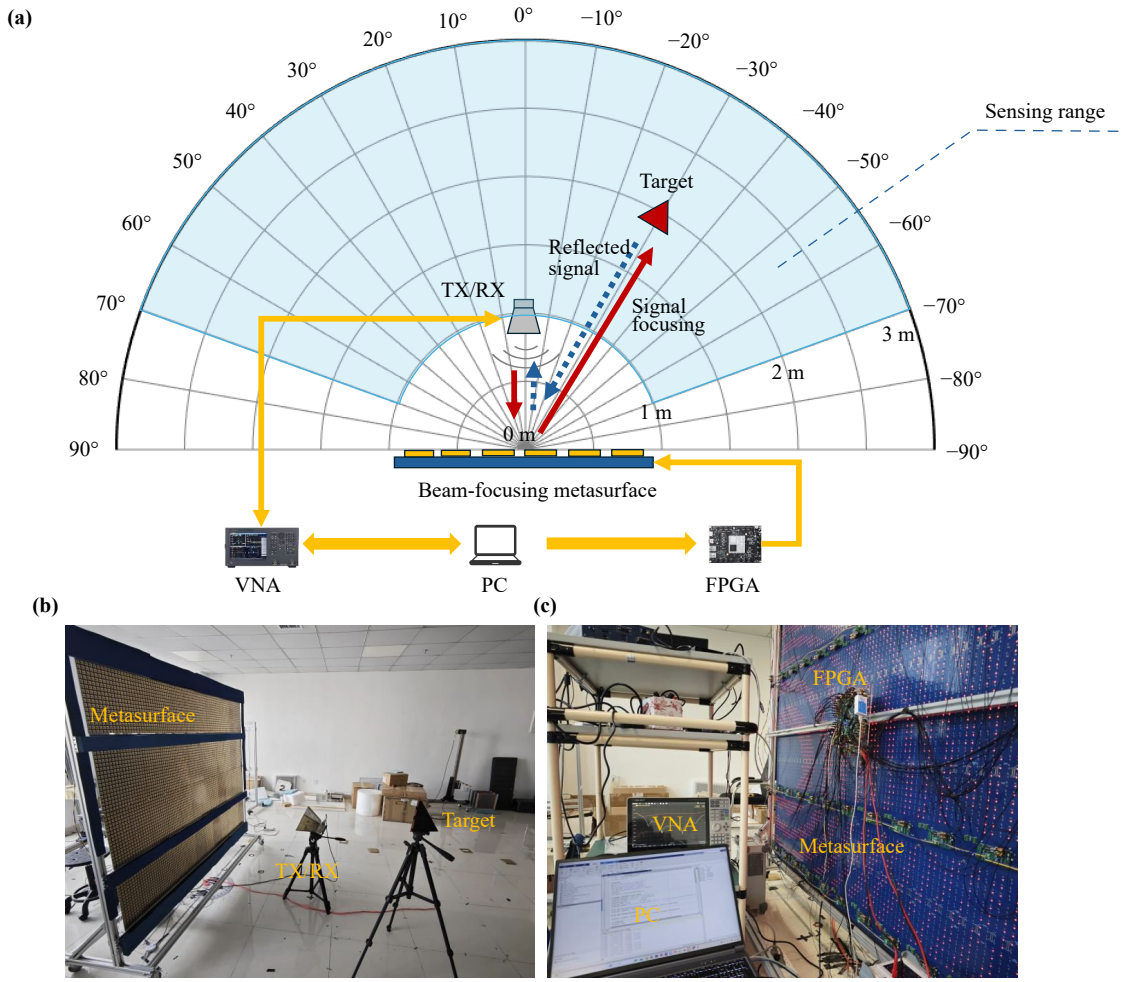

Fig. 3 System block diagram and experimental setup. **(a)** Operational block diagram, including definitions of target azimuth angle and distance. The blue region indicates the target sensing area. **(b)** Experimental setup in front of the metasurface. The co-located transmit-receive antenna is tilted upward, and the target height is aligned with the metasurface's central height. **(c)** Experimental setup behind the metasurface. The PC is connected to both the vector network analyzer and the FPGA to acquire reflected signal strength data and to transmit coding sequences. The coding state can be visually monitored via the on/off status of LEDs mounted on the back of the units.

thereby enhancing the reliability and robustness of the sensing results. Before target detection, the same measurement procedure is conducted under no-target conditions to collect environmental noise data. These samples are then used to construct an angle-dependent noise threshold for subsequent target-presence decisions (detailed in Section 3).

Upon completion of the full angular scan, a peak search is conducted on the obtained average reflection strength curve, and the peak value is compared with the noise threshold corresponding to the respective angle. If the peak value is below the threshold, it is determined that there is no target. Otherwise, it is determined that a target has been detected, and the angle corresponding to the peak value is identified as the target azimuth. After acquiring the angular information of the target, the focusing direction is fixed at that angle, and a distance scan is carried out from 1 m to 3 m in 0.1 m steps. At each distance, the mean reflected strength is again measured, and peak detection is applied. The distance corresponding to the maximum strength is recorded as the target distance. Since target presence has already been confirmed during the angular scan, no additional threshold comparison is required. This entire sensing procedure is implemented in software and executed automatically.

The system's operational block diagram is presented in Fig. 3(a), and the experimental setup is shown in Figs. 3(b) and (c). The PC connected to the FPGA via a data communication interface computes the metasurface coding corresponding to the desired focal position and transmits it to the FPGA. In the experiment, the target (a corner reflector) is placed within the horizontal plane that passes through the center of the metasurface. Its

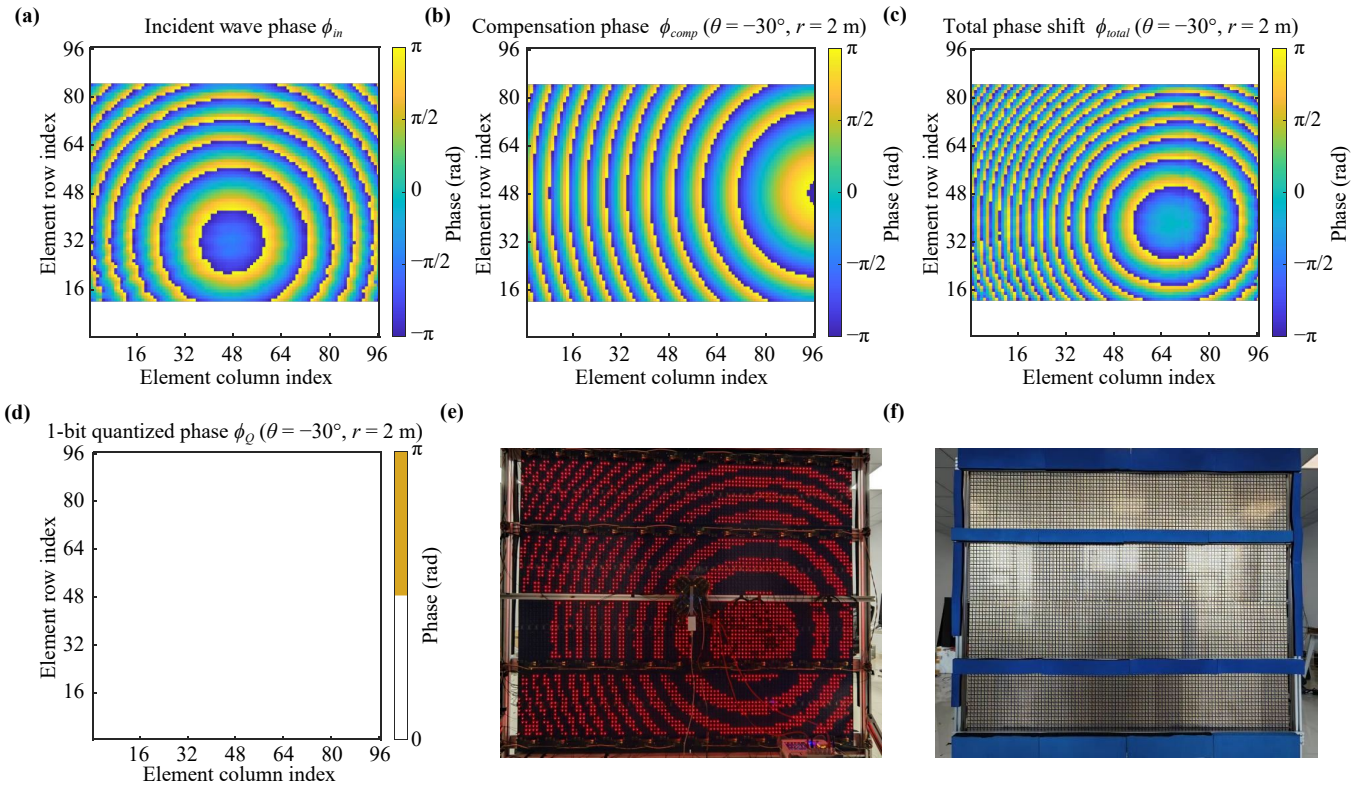

Fig. 4 Illustration of the incident phase distribution and coding. **(a)** Incident wave phase distribution. **(b)** Computed compensation phase for focusing. **(c)** Computed total phase shift. **(d)** 1-bit quantized phase. **(e)** Actual coding distribution of the metasurface elements, where the discontinuous regions contain no unit cells. **(f)** Front view of the metasurface, where regions obscured by wave-absorbing material contain no unit cells.

distance from the metasurface center is r, forming an angle θ with the surface normal, the target may move freely within this plane. The distributions of azimuth angle and distance are shown in Fig. 3(a). A dual-function transmit-receive antenna is positioned 1 m directly in front of the metasurface center, corresponding to $r = 1$m and $\theta = 0°$. The antenna is connected via coaxial cable to a vector network analyzer (Keysight SNA5032A), which supplies the incident signal (set to a default power of 0 dBm) and captures the reflected echo. The antenna is positioned slightly below the center height of the metasurface and tilted upward at a certain elevation angle, as shown in Fig. 3(b), to avoid potential interference when the target azimuth angle is near 0°. To mitigate interference between the transmit and receive paths, the reflected echo is extracted using the time-domain gating (time-windowing) function of the vector network analyzer (VNA). Since the sensing range is restricted to targets located within 1–3 m, only the reflected signals within the corresponding time-delay window are retained. As a result, the reflected-strength response used for subsequent peak searching is dominated by the target echo, ensuring reliable target localization.

The metasurface comprises a 64 × 96 array of unit cells with a period of 20 mm, designed to operate at 3.4 GHz, as shown in Fig. 3(b). The large-scale nature of the metasurface array mitigates the impact of phase-quantization errors on system performance, thereby enhancing the accuracy and stability of target sensing. Each metasurface unit is equipped with a light-emitting diode (LED) indicator on the backside, which lights up to indicate that the current encoding is "1" and turns off to indicate that the encoding is "0". During operation, the overall coding distribution of the metasurface can be visually monitored via the LED pattern on its backside, as shown in Fig. 3(c).

Since the feeding antenna is situated in the metasurface's near-field region and is inclined at a certain elevation angle, the phase distribution of its transmitted wave upon reaching the metasurface cannot be determined accurately through theoretical calculation. To ensure the precision of the total compensation phase, a scanning rig was used to directly measure the incident wave phase ϕ_{in} at each metasurface element. The measurement results are shown in Fig. 4(a), where rows 1–12 and 85–96 contain no unit cells. Taking the focal point at r = 2 m and θ = –30° as an example, Figs. 4(b)–(e) respectively illustrate the compensation phase ϕ_{comp}, the total phase shift ϕ_{total}, the 1-bit quantized phase ϕ_Q, and the resulting metasurface element coding distribu-

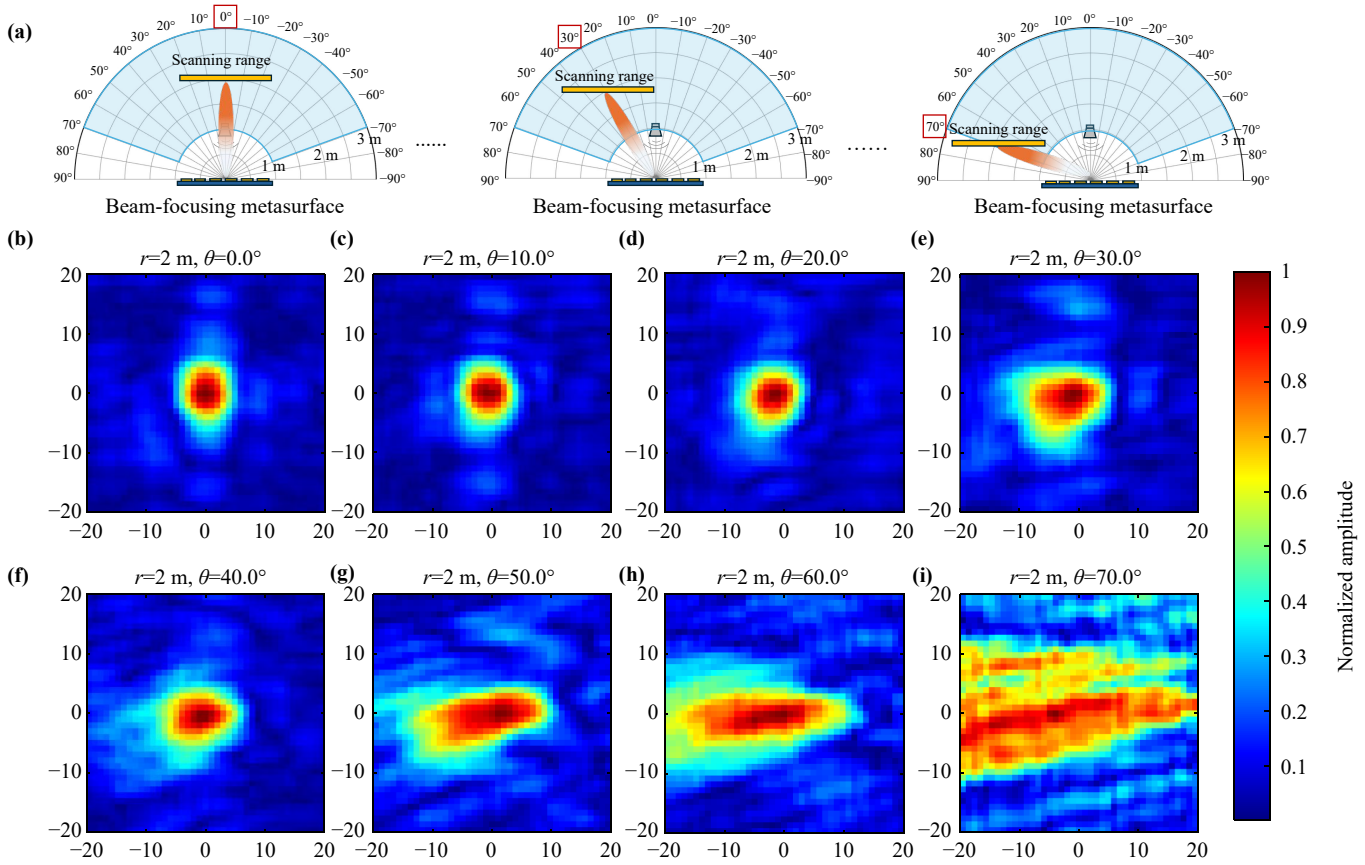

Fig. 5 Illustration of the scanning range and focus spot electric field strength distribution scan results. **(a)** Illustration of the scanning range. The scanning rig was placed parallel to the metasurface and aligned with the focal point center. **(b–i)** correspond to the focus spot electric field strength distribution at focusing angles θ = 0°, 10°, 20°, 30°, 40°, 50°, 60°, and 70°, respectively. The scanning area is a 0.8 m × 0.8 m plane centered around the focus, with a spatial resolution of 20 mm. The color scale represents the magnitude of the electric field strength, normalized to a maximum value of 1.

tion. In Fig. 4(e), the discontinuous regions contain no unit cells, which correspond to the areas masked by wave-absorbing material in Fig. 4(f).

3 Results and discussion

To verify the focusing performance of the metasurface, a near-field scan of the focus spot was conducted first. In the experiment, the focusing distance was fixed at 2 m, and the focusing angle varied from 0° to 70° with a step size of 10°. At each angle, the scanning rig was placed parallel to the metasurface and aligned with the focal point center, as illustrated in Fig. 5(a). A probe was used to collect the electric field strength at each point within a 0.8 m × 0.8 m planar area with a spatial resolution of 20 mm, resulting in 8 sets of data. The focus spot electric field strength distribution is shown in Figs. 5(b)–(i).

The scanning results indicate that as the focusing angle increases, the focusing performance of the metasurface gradually decreases, which may lead to a reduction in the detection accuracy of edge targets and increase the risk of false detection regarding target existence. To accurately determine whether a target is present or not, it is necessary to pre-establish an environmental noise threshold, as illustrated in Fig. 6(a). First, with no target present, the focal distance is fixed at 2 m, and a full azimuth scan is performed from –70° to 70° in 0.2° increments. At each scan angle, the mean reflected signal strength is measured and recorded using the method described above. This process is repeated multiple times, and the average of all measurement results is taken as the noise floor. In the measurement setup, the aggregate noise can be approximated as Gaussian. By statistical convention, where approximately 99.7% of Gaussian samples lie within $\mu \pm 3\sigma$, the noise threshold for each angle was set as the noise floor plus three times the standard deviation σ. Using statistical values to define the threshold mitigates the impact of sporadic interference and measurement jitter. In the experiment, a target is considered present only when the peak value exceeds the corresponding threshold. Although noise may occasionally rise above the threshold at individual

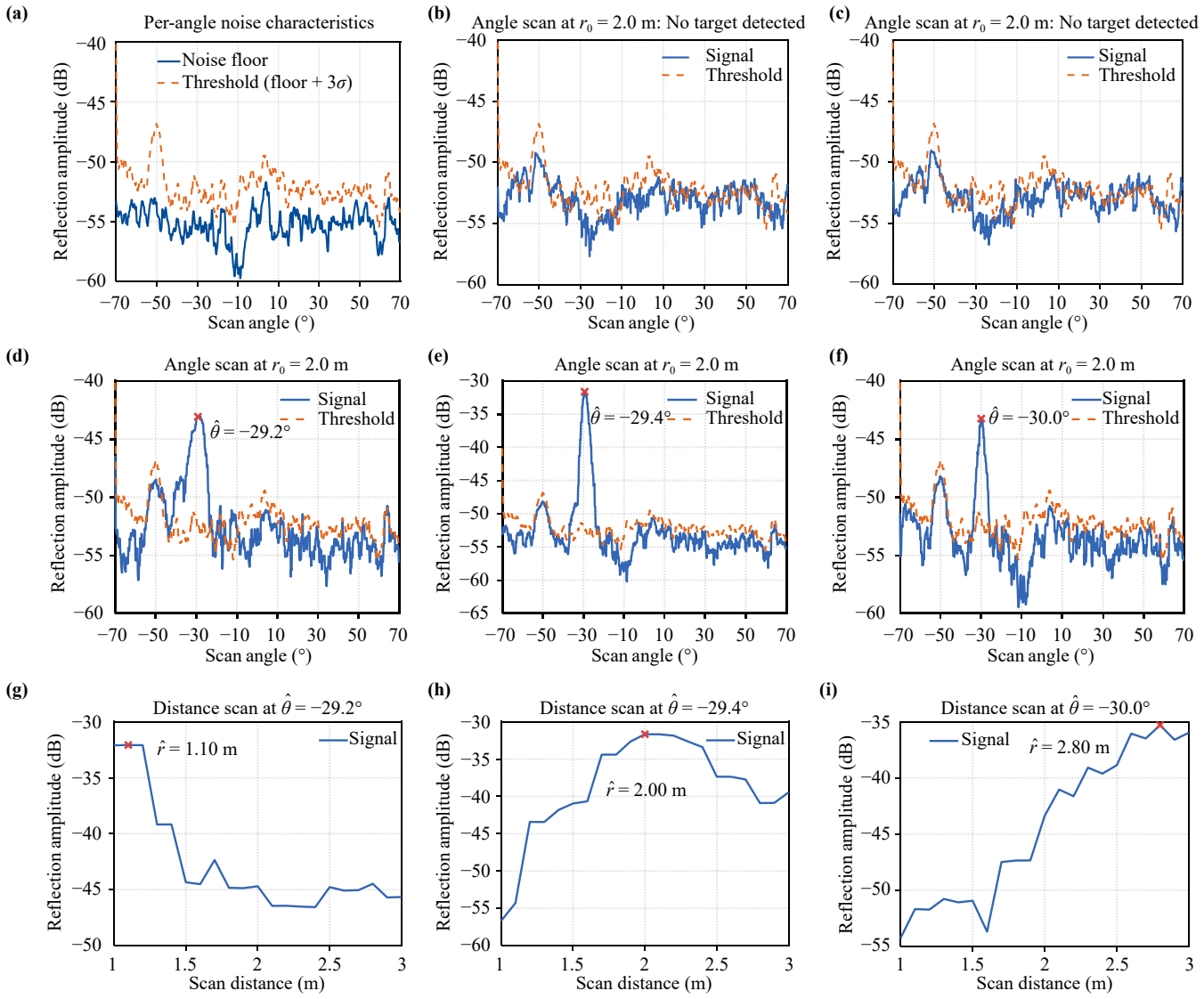

Fig. 6 Environmental noise threshold and sensing result examples, where the blue curve represents the measured reflection signal strength, and the orange curve represents the noise threshold. **(a)** Noise floor curve and threshold curve. **(b, c)** Angle scan results under no-target conditions. **(d–f)** Angle scan results for three samples at $\theta = -30°$, $r = 1$ m, 2 m, and 3 m. **(g–i)** Distance scan results for three samples at $\theta = -30°$, $r = 1$ m, 2 m, and 3 m.

angles under no-target conditions, a target is considered present only if the "peak" condition is met, thereby improving robustness against environmental fluctuations. Figs. 6(b) and (c) show example angle-scan results under no-target conditions. It can be seen that the noise exceeds the threshold at certain angles, yet both are correctly identified as "no target".

To validate the feasibility of the proposed passive target sensing method, experiments were conducted at a total of 74 discrete positions. Specifically, the azimuth angle was sampled from –70° to 70° in 10° increments, and the distance was sampled from 1 m to 3 m in 0.5 m increments, yielding 75 positions in total. The point at $r = 1$ m and $\theta = 0°$ was excluded because the antenna occupied that location, leaving 74 effective test points. Figures 6(d)–(i) select three samples at $\theta = -30°$, with distances $r = 1$ m, 2 m, and 3 m, as typical examples. The corresponding angle scan curves and distance scan curves are shown, with the estimated azimuth angles and distances labeled in the figures.

From the plots, the estimated angles for the three samples are –29.2°, –29.4°, and –30.0°, corresponding to errors of 0.8°, 0.6°, and 0.0°, respectively. The estimated distances are 1.1 m, 2.0 m, and 2.8 m, with errors of 0.1 m, 0.0 m, and –0.2 m, respectively, demonstrating the high-precision two-dimensional sensing capability of the proposed method. Figures 7(a) and (d) respectively show the distribution of angle and distance estimation errors for all samples. The point at $r = 1$ m and $\theta = 0°$ was excluded because it is occupied by the antenna, leaving

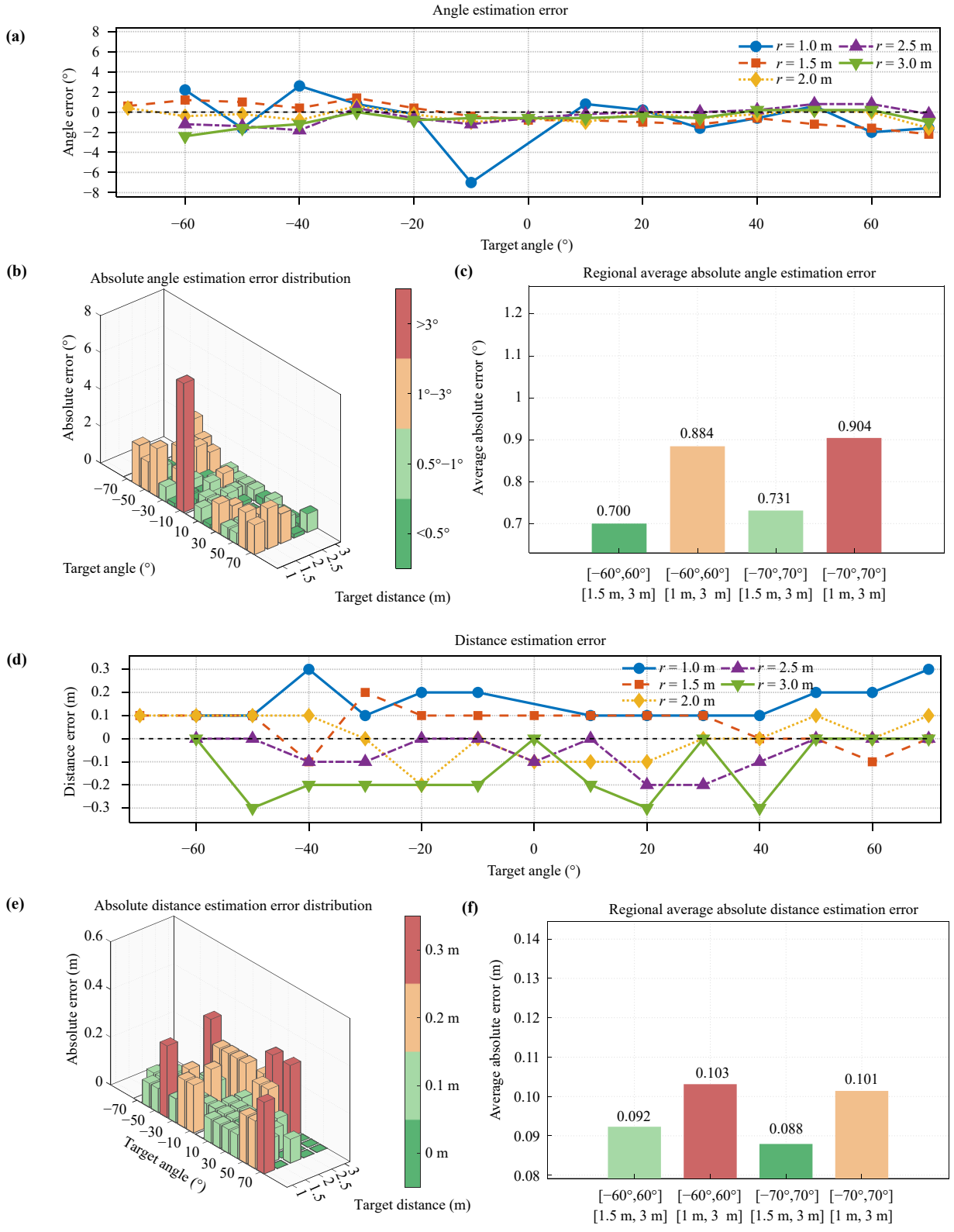

Fig. 7 Sensing error distribution and regional performance comparison. **(a)** Distribution of angle estimation errors for all valid samples (excluding the antenna occupation point). **(b)** Histogram of absolute angle estimation errors for valid samples. **(c)** Comparison of average absolute angle estimation errors for different regions (including and excluding the edge distance $r = 1$ m, and including and excluding extreme angles $\theta = \pm 70°$). **(d)** Distribution of distance estimation errors for all valid samples. **(e)** Histogram of absolute distance estimation errors for valid samples. **(f)** Comparison of average absolute distance estimation errors for different regions.

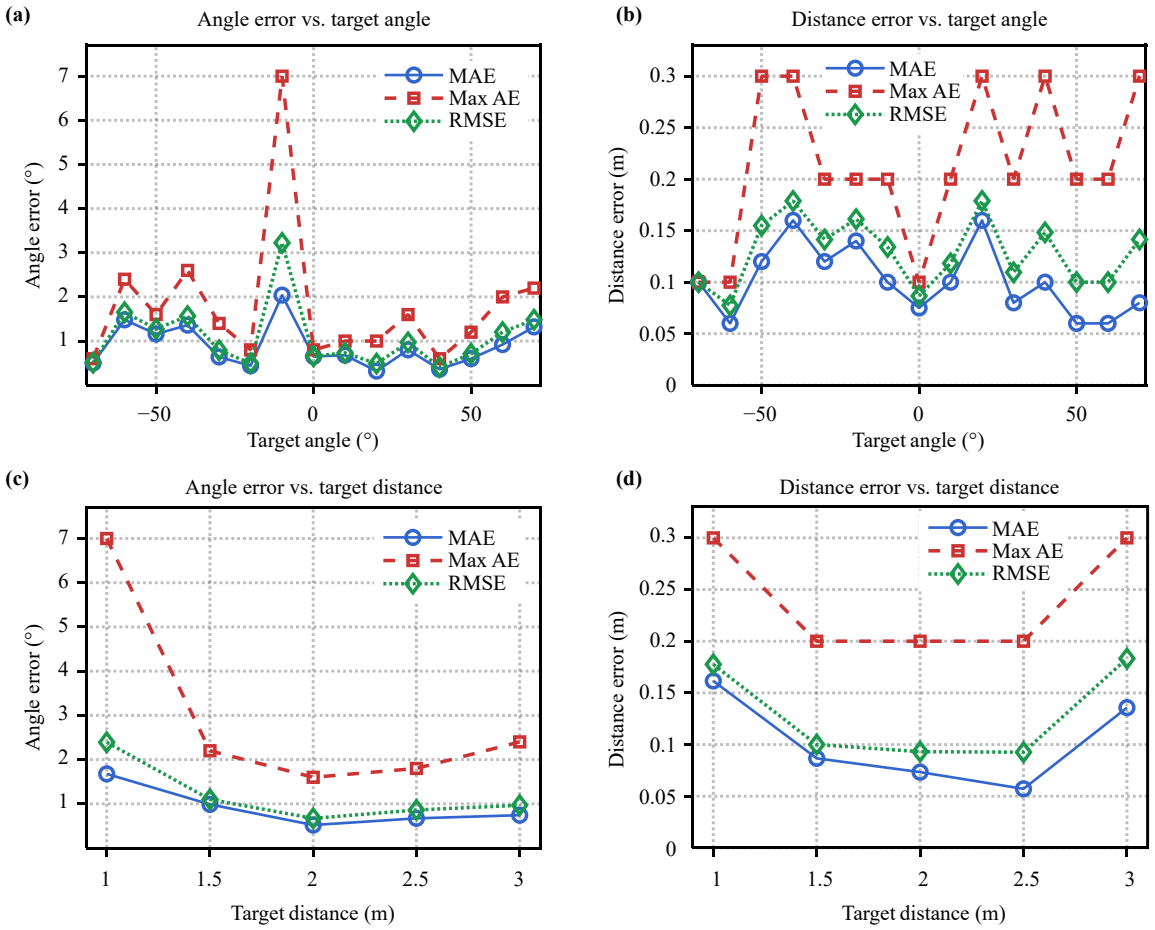

Fig. 8 Trends of absolute estimation errors with variations in target azimuth angle and distance. **(a)** Trend of absolute angle estimation error with changes in target azimuth angle. **(b)** Trend of absolute distance estimation error with changes in target azimuth angle. **(c)** Trend of absolute angle estimation error with changes in target distance. **(d)** Trend of absolute distance estimation error with changes in target distance.

74 samples in total. Among these, three samples at $\theta = 70°$ with $r = 1$ m, 2.5 m, and 3 m were misclassified as "no target". This was primarily attributable to the degradation of the metasurface's focusing performance in the edge regions, resulting in the reflected signal peaks failing to exceed the noise threshold. The remaining 71 samples were correctly identified, resulting in an overall detection accuracy of 95.95%. Figures 7(b) and (e) show the distribution of absolute angle and distance estimation errors for 71 valid samples. For absolute angle estimation errors, 24 samples have an error of less than 0.5°, 50 samples have an error of less than 1°, and 70 samples have an error of less than 3°. For absolute distance estimation errors, all samples do not exceed 0.3 m, with 22 samples having an error of 0 m, 31 samples having an error of 0.1 m, 13 samples having an error of 0.2 m, and 5 samples having an error of 0.3 m. Overall, the results show that the system provides high measurement accuracy in both the angle and distance dimensions. As shown in Fig. 7(a), a sample located at $r = 1$ m, $\theta = -10°$ exhibits a significant angle estimation error of −7°, primarily because the target is close to the metasurface, causing local obstruction and interference with the incident wave, thereby weakening the focusing effect. Notably, Fig. 7(d) shows that the distance estimation error for this sample is only 0.2 m, indicating that the angle estimation error did not significantly affect the distance measurement.

To further assess the performance differences of the proposed method in edge and non-edge regions, Figs. 7(c) and (f) compare the average absolute angle and distance estimation errors for samples from different regions (including and excluding edge distance $r = 1$ m, and including and excluding extreme angles $\theta = \pm 70°$). The results indicate that samples with $r = 1$ m have higher absolute angle and distance estimation errors compared to those located farther from the metasurface. This occurs because fixing the initial focal distance at 2 m during the angle scan stage hinders the detection of nearby targets. Moreover, very close targets also disrupt the incident wave, further degrading focusing performance. However, the absolute angle and distance esti-

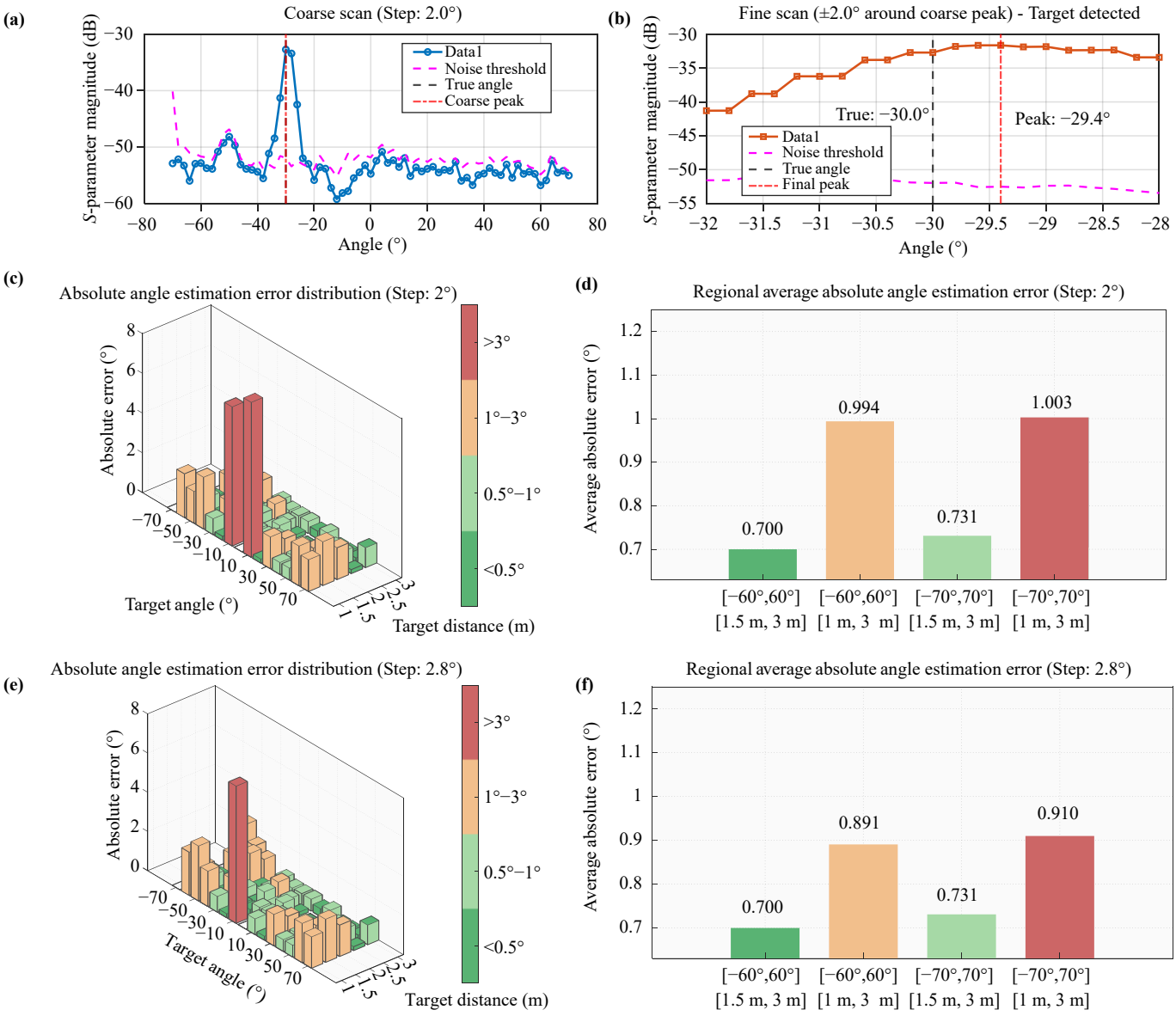

Fig. 9 Multi-resolution angular scanning strategy and performance evaluation. **(a)** Coarse angular scanning curve for a representative sample located at $\theta = -30°$ and $r = 2$ m. **(b)** Corresponding fine scanning curve around the main lobe. **(c)** Absolute angle estimation error distribution with a coarse scanning step size of 2°. **(d)** Regional average absolute angle estimation error with a coarse scanning step size of 2°. **(e)** Absolute angle estimation error distribution with a coarse scanning step size of 2.8°. **(f)** Regional average absolute angle estimation error with a coarse scanning step size of 2.8°.

mation errors of the samples with $\theta = \pm 70°$ are comparable to those at intermediate angles. This suggests that while the sensing accuracy drops slightly for very close objects, this method still maintains high accuracy for targets with large angles.

Figure 8 summarizes the trends of absolute angle and distance estimation errors as functions of target azimuth angle and distance, providing a more intuitive assessment of how target position affects sensing accuracy. The performance metrics shown include the mean absolute error (MAE), maximum absolute error (Max AE), and root mean square error (RMSE). As shown in Figs. 8(a) and (b), variations in target azimuth angle have no significant impact on angle and distance estimation accuracy. However, Figs. 8(c) and (d) indicate that when the target is too close or too far from the metasurface, both angle and distance estimation errors increase, suggesting that the target distance and the preset initial scanning distance play a critical role in sensing performance.

In summary, out of 74 total test samples, 71 samples were successfully detected, yielding a target recognition accuracy of 95.95%. For these 71 valid samples, the mean absolute error of angle estimation was 0.904°, and

the mean absolute error of distance estimation was 0.101 m. These results fully demonstrate that the proposed passive target sensing method enables high-precision two-dimensional measurement of angle and distance over a wide detection range.

Considering that the angular response around the target typically exhibits a pronounced main lobe, a multi-resolution coarse-to-fine scanning strategy can be introduced to further improve the sensing efficiency. Specifically, a coarse scan with a relatively large step size is first performed over the entire angular range, followed by a fine scan with a smaller step size within a limited angular region around the main lobe. This strategy is expected to significantly reduce the number of sampling points while maintaining localization accuracy, thereby improving the overall measurement efficiency.

The effectiveness of this approach has been validated using the collected data. Representative angular scanning curves are shown in Figs. 9(a) and (b), where the proposed strategy achieves the same peak location as the full-resolution scan while substantially reducing the number of sampling points. Furthermore, simulations based on measured data with coarse step sizes of 2° and 2.8° are conducted, and the corresponding error statistics are presented in Figs. 9(c)–(f). Future work will further investigate this strategy to enhance the real-time performance and practical applicability of the proposed sensing system.

4 Conclusion

This paper presents a passive target-sensing system that combines a beam-focusing algorithm with a programmable metasurface. An FPGA dynamically reconfigures the metasurface's coding patterns in real time to perform focused-beam scanning. The system acquires reflected signal strength via a single RF channel to estimate target angle and distance, offering a simple architecture and low computational complexity. Experiment results show that the proposed method can achieve high-precision, reliable, and robust sensing within a range of –70° to 70° azimuth and 1 m to 3 m distance. We believe this work can be further expanded into multi-target scenarios, integrate additional functions, and explore performance in non-ideal environments, thereby promoting the widespread application of programmable metasurface sensing technology in intelligent wireless networks, medical detection, and other fields.

Declarations The authors have no conflicts to disclose.

Data availability The data that support the findings of this study are available from the corresponding author upon reasonable request.

Acknowledgements This work was supported by the National Key Research and Development Program of China (No. 2022YFA1404903), the Special Fund for Key Basic Research in Jiangsu Province (No. BK20243015), Jiangsu Joint Laboratory of Multidimensional Perceptual Information Technology (No. BM2022017), the National Natural Science Foundation of China (Nos. 92167202, 62301147, and 62288101), the Natural Science Foundation of Jiangsu Province (No. BK20230822), the Major Project of Natural Science Foundation of Jiangsu Province (Nos. BK20212002 and BK20210209), the Young Elite Scientists Sponsorship Program by CAST (No. 2022QNRC001), the State Key Laboratory of Millimeter Waves, Southeast University, China (No. K201924), the Fundamental Research Funds for the Central Universities (Nos. 2242023K5002, 2242018R30001, and 2242022R20017), the 111 Project (111-2-05), and the China Postdoctoral Science Foundation (Nos. 2021M700761 and 2022T150112).

References

1. Q. Ma, Z. L. Mei, S. K. Zhu, T. Y. Jin, and T. J. Cui, Experiments on active cloaking and illusion for Laplace equation, *Phys. Rev. Lett.* 111(17), 173901 (2013)
2. Q. Ma and T. J. Cui, Information metamaterials: bridging the physical world and digital world, *PhotoniX* 1(1), 1 (2020)
3. Q. R. Hong, Q. Ma, X. X. Gao, C. Liu, Q. Xiao, S. Iqbal, and T. J. Cui, Programmable amplitude-coding metasurface with multifrequency modulations, *Adv. Intell. Syst.* 3(8), 2000260 (2021)
4. Q. Ma, C. Liu, Q. Xiao, Z. Gu, X. Gao, L. Li, and T. J. Cui, Information metasurfaces and intelligent metasurfaces, *Photon. Insights* 1(1), R01 (2022)
5. Y. M. Ning, Q. Ma, Q. Xiao, Z. Gu, and T. J. Cui, Reprogrammable nonlinear transmission controls using an information metasurface, *Adv. Opt. Mater.* 12(3), 2301525 (2024)
6. V. G. Veselago, The electrodynamics of substances with simultaneously negative values of and, *Sov. Phys. Usp.* 10(4), 509 (1968)
7. J. B. Pendry, A. J. Holden, W. J. Stewart, and I. Youngs, Extremely low frequency plasmons in metallic mesostructures, *Phys. Rev. Lett.* 76(25), 4773 (1996)
8. J. B. Pendry, Negative refraction makes a perfect lens, *Phys. Rev. Lett.* 85(18), 3966 (2000)
9. T. J. Cui, M. Q. Qi, X. Wan, J. Zhao, and Q. Cheng, Coding metamaterials, digital metamaterials and programmable metamaterials, *Light Sci. Appl.* 3(10), e218 (2014)
10. L. Chen, Q. Ma, Q. F. Nie, Q. R. Hong, H. Y. Cui, Y. Ruan, and T. J. Cui, Dual-polarization programmable metasurface modulator for near-field information encoding and transmission, *Photon. Res.* 9(2), 116 (2021)
11. L. Chen, Q. Ma, S. S. Luo, F. J. Ye, H. Y. Cui, and T. J. Cui, Touch-programmable metasurface for various electromagnetic manipulations and encryptions, *Small* 18(45), 2203871 (2022)
12. Q. Ma, G. D. Bai, H. B. Jing, C. Yang, L. Li, and T. J. Cui, Smart metasurface with self-adaptively reprogrammable functions, *Light Sci. Appl.* 8(1), 98 (2019)
13. Q. Ma, Q. R. Hong, X. X. Gao, H. B. Jing, C. Liu, G. D. Bai, Q. Cheng, and T. J. Cui, Smart sensing metasurface with self-defined functions in dual polarizations,

Nanophotonics 9(10), 3271 (2018)
14. R. Z. Jiang, Q. Ma, Z. Gu, J. C. Liang, Q. Xiao, Q. Cheng, and T. J. Cui, Simultaneously intelligent sensing and beamforming based on an adaptive information metasurface, *Adv. Sci. (Weinh.)* 11(7), 2306181 (2024)
15. W. Li, Q. Ma, C. Liu, Y. Zhang, X. Wu, J. Wang, S. Gao, T. Qiu, T. Liu, Q. Xiao, J. Wei, T. T. Gu, Z. Zhou, F. Li, Q. Cheng, L. Li, W. Tang, and T. J. Cui, Intelligent metasurface system for automatic tracking of moving targets and wireless communications based on computer vision, *Nat. Commun.* 14(1), 989 (2023)
16. W. Tang, M. Z. Chen, X. Chen, J. Y. Dai, Y. Han, M. Di Renzo, Y. Zeng, S. Jin, Q. Cheng, and T. J. Cui, Wireless communications with reconfigurable intelligent surface: Path loss modeling and experimental measurement, *IEEE Trans. Wirel. Commun.* 20(1), 421 (2021)
17. L. Zhang and T. J. Cui, Space-time-coding digital metasurfaces: Principles and applications, *Research* 2021, 9802673 (2021)
18. Q. Xiao, W. Gao, Q. Ma, Z. Gu, Y. Zhou, C. Liu, Z. A. Huang, X. Wan, L. Li, Y. Li, and T. J. Cui, Electromagnetic brain-computer-metasurface holography, *ACS Photonics* 10(7), 2249 (2023)
19. L. Li, Y. Shuang, Q. Ma, H. Li, H. Zhao, M. Wei, C. Liu, C. Hao, C. W. Qiu, and T. J. Cui, Intelligent metasurface imager and recognizer, *Light Sci. Appl.* 8(1), 97 (2019)
20. J. W. You, Q. Ma, Z. Lan, Q. Xiao, N. C. Panoiu, and T. J. Cui, Reprogrammable plasmonic topological insulators with ultrafast control, *Nat. Commun.* 12(1), 5468 (2021)
21. Q. Ma, W. Gao, Q. Xiao, Z. Ding, T. Gao, Y. Zhou, X. Gao, T. Yan, C. Liu, Z. Gu, X. Kong, Q. H. Abbasi, L. Li, C. W. Qiu, Y. Li, and T. J. Cui, Directly wireless communication of human minds via non-invasive brain-computer-metasurface platform, *eLight* 2(1), 11 (2022)
22. C. Liu, Q. Ma, Z. J. Luo, Q. R. Hong, Q. Xiao, H. C. Zhang, L. Miao, W. M. Yu, Q. Cheng, L. Li, and T. J. Cui, A programmable diffractive deep neural network based on a digital-coding metasurface array, *Nat. Electron.* 5(2), 113 (2022)
23. X. Gao, Q. Ma, Z. Gu, W. Y. Cui, C. Liu, J. Zhang, and T. J. Cui, Programmable surface plasmonic neural networks for microwave detection and processing, *Nat. Electron.* 6(4), 319 (2023)
24. X. Gao, Z. Gu, Q. Ma, B. J. Chen, K. M. Shum, W. Y. Cui, J. W. You, T. J. Cui, and C. H. Chan, Terahertz spoof plasmonic neural network for diffractive information recognition and processing, *Nat. Commun.* 15(1), 6686 (2024)
25. Z. Gu, Q. Ma, X. Gao, J. W. You, and T. J. Cui, Direct electromagnetic information processing with planar diffractive neural network, *Sci. Adv.* 10(29), eado3937 (2024)
26. H. Krim and M. Viberg, Two decades of array signal processing research: The parametric approach, *IEEE Signal Process. Mag.* 13(4), 67 (1996)
27. R. Schmidt, Multiple emitter location and signal parameter estimation, *IEEE Trans. Antenn. Propag.* 34(3), 276 (1986)
28. R. Roy and T. Kailath, ESPRIT-estimation of signal parameters via rotational invariance techniques, *IEEE Trans. Acoust. Speech Signal Process.* 37(7), 984 (1989)
29. M. Lin, M. Xu, X. Wan, H. Liu, Z. Wu, J. Liu, B. Deng, D. Guan, and S. Zha, Single sensor to estimate DOA with programmable metasurface, *IEEE Internet Things J.* 8(12), 10187 (2021)
30. X. Q. Chen, L. Zhang, S. Liu, and T. J. Cui, Artificial neural network for direction-of-arrival estimation and secure wireless communications via space-time-coding digital metasurfaces, *Adv. Opt. Mater.* 10(23), 2201900 (2022)
31. J. Y. Dai, W. Tang, M. Wang, M. Z. Chen, Q. Cheng, S. Jin, T. J. Cui, and C. H. Chan, Simultaneous in situ direction finding and field manipulation based on space-time-coding digital metasurface, *IEEE Trans. Antenn. Propag.* 70(6), 4774 (2022)
32. X. Fang, M. Li, J. Han, D. Ramaccia, A. Toscano, F. Bilotti, and D. Ding, Accurate direction-of-arrival estimation method based on space-time modulated metasurface, *IEEE Trans. Antenn. Propag.* 70(11), 10951 (2022)
33. Q. Zhou, S. Wang, J. Dai, and Q. Cheng, Simultaneous direction of arrival estimation and radar cross-section reduction based on space-time-coding digital metasurfaces, *J. Radars* 13(1), 150 (2024)
34. X. Wang and C. Caloz, Direction-of-arrival (DOA) estimation based on spacetime-modulated metasurface, in: *2019 IEEE Int. Symp. Antennas Propag. USNC-URSI Radio Sci. Meet.*, 1613 (2019)
35. D. Xia, X. Wang, J. Han, H. Xue, G. Liu, Y. Shi, L. Li, and T. J. Cui, Accurate 2-D DoA estimation based on active metasurface with nonuniformly periodic time modulation, *IEEE Trans. Microw. Theory Tech.* 71(8), 3424 (2023)